Atinafu *et al. Biochar* (2026) 8:6
https://doi.org/10.1007/s42773-025-00517-4

Biochar

ORIGINAL RESEARCH Open Access

Engineered mineral-doped biochar-infused paraffin for synergistic enthalpy storage and enhanced thermal management

Dimberu G. Atinafu[1], Jihee Nam[1] and Sumin Kim[1*]

Abstract

The design of phase-change renewable energy-harvesting materials has garnered increasing attention for achieving sustainable energy infrastructure and advanced applications. However, energy storage density that relies on the shape and crystallization of pristine phase-change materials (PCMs) usually lacks charge/discharge efficiency, and the inherent lattice defects in individual supporting scaffolds, further constrain their overall performance. In this study, lignocellulose-based biochar (obtained from spruce thermolysis at 600 °C) was assembled with an organically intercalated montmorillonite (MT) via modification and ultrasonication-assisted vacuum drying to produce engineered biomineral-based composite PCMs that simultaneously improve the latent heat and crystallinity of paraffin PCM. The biomineral hybrid was prepared using two preparation techniques: a conventional method of integrating biochar with clay mineral without intercalation, and a structural engineering approach involving the doping of cationic nanoclay into biochar. The engineered hybrid (EMB) achieved a 516.4% increase in surface area (9.9 $m^2\ g^{-1}$ for bulk MT) and demonstrated a high PCM adsorption rate for hexadecane (C_{16}) with 223.3% enhancement in latent heat (15.7 to 121.3 $J\ g^{-1}$). The composite (EMB@C_{16}) also exhibited a 78% enhancement of thermal conductivity and charging/discharging efficiency. Moreover, EMB@C_{16} retained over 95.9% of latent heat after 1000 cycles of heating (50 °C) and cooling (23 °C), with only a 4.1% reduction, providing continuous thermal energy supply during real-time temperature variation evaluations with thermal infrared imaging under both short and long cycle durations. This fabrication technique provides a rational approach for integrating naturally sourced and thermophysically reinforced biochar-based hybrids for advanced thermal regulation systems.

Highlights

- Lignocellulose biochar was combined with cationic nanoclay for paraffin adsorption via encapsulation technology, enabling simultaneous energy storage and enhanced durability.
- The thermal performance of biomineral composites was evaluated following two distinct design strategies.
- EMB@C16, an engineered mineral-doped biochar, exhibited 223.3% of the energy storage capacity of bulk material.

Keywords Biochar, Nanoclay, Modification, Thermal energy storage, Reliability

*Correspondence:
Sumin Kim
kimsumin@yonsei.ac.kr

Graphical Abstract

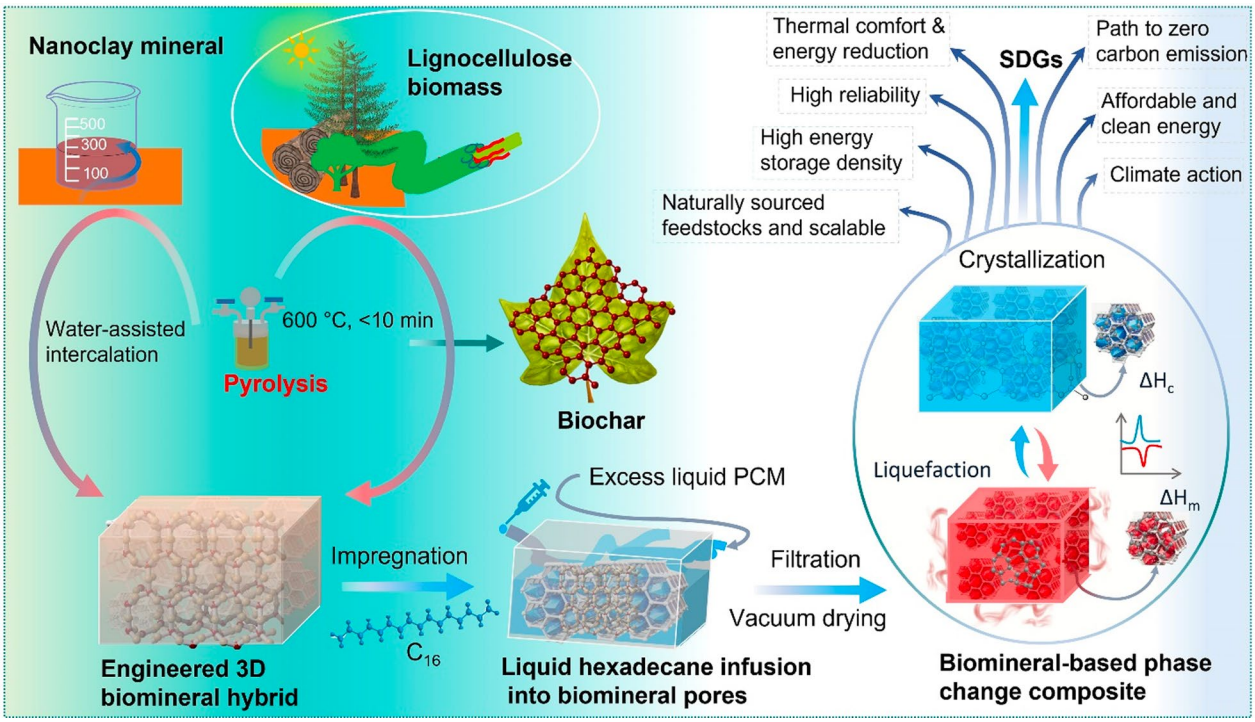

1 Introduction

The use of latent heat storage in phase change materials (PCMs) is crucial in the engineering of thermal energy harvesting, transformation, and management, with significant advantages in balancing rapid energy supply and consumption (Qiu et al. 2025). The reversible energy charging/discharging, isothermal phase change temperature, corrosion-free nature, non-toxicity, and low subcooling characteristics of organic PCMs provide promising performance in diverse advanced applications, such as heat signal camouflage (Li et al. 2023a, b), photo thermoelectric conversion for photovoltaic power generation (Liu et al. 2024), personal thermal climate management (Liu et al. 2019), and other thermal regulation and energy storage (Li et al. 2023a, b). However, numerous shortcomings of pristine PCMs, such as liquid-phase seepage and insufficient energy conversion capability, considerably limit the broader applications of PCMs. To address these problems, researchers have focused on integrating PCMs with fossil fuel-derived carbon materials, such as graphene and carbon nanotubes, metallic nanomaterials, and biomimetic technologies, and developing composites with excellent thermophysical properties as phase-change composites (Liu et al. 2023). For instance, bean-pod-inspired 3D-printed phase change microlattices, constructed using graphene and octadecane, offer high transversal thermal transport of 1.67 W m^{-1} K^{-1} and latent heat of 190 J g^{-1} with 99.1% preservation after multiple heating–cooling cycles (Yang et al. 2021). However, challenges persist owing to the high cost, complicated design process, inadequate energy harvesting capability, unsatisfactory thermal conductivity, and even poor shape-stability of composite materials.

Recently, biochar produced through the anoxic thermochemical conversion of biomaterials (Lehmann et al. 2021) has been used as a carrier for PCMs and offers high thermal stability in composite PCMs (Atinafu et al. 2024a, b; Lv et al. 2024). However, the trade-off between PCM impregnation efficiency and reversible crystallizability presents challenges and is presumably unsuitable for operational applications (Aftab et al. 2024). Although the PCM/biochar composite is still in early development stages, studies have shown inadequate energy storage (< 100 J g^{-1}) and low PCM encapsulation efficiency (< 50%) (Atinafu et al. 2024a, b). In addition to the limited pore area, the strong surface intermolecular interaction between PCMs (primary reactive functional groups) and biochar is considered a crucial factor, as a 1-dodecanol/biochar results in a lower phase change enthalpy (56.2 J g^{-1}) than an n-dodecane/biochar, which exhibits

up to 90.5 J g^{-1} (Atinafu et al. 2020). Therefore, further advancing the employment of biochar in thermal energy storage is imperative. Specifically, the fabrication of composite PCMs with an integrated eco-friendly and porous structure offers numerous prospects and challenges for fulfilling advanced thermal management demands. Tailoring the pore characteristics and surface functionalization of PCMs carrier materials has proven effective in improving the adsorption efficiency and energy harvesting capability of phase-transition composites (Wang et al. 2016).

Interestingly, natural mineral materials, such as montmorillonite (MT), glauconite, chlorite, halloysite, and palygorskite, can provide advantages in addition to addressing the inherent challenges of PCMs owing to their outstanding capturing capacity, cost-effectiveness, and eco-friendliness. Of particular interest is MT, comprising a 2:1 (T–O–T) structure, an alumina octahedral (O) layer sandwiched between two silica tetrahedral (T) layers—a naturally occurring layered silicate mineral featuring abundant microporous interlayer and interparticle pores (Shi et al. 2023). However, its extremely inadequate PCM adsorption capacity and shape stability performance, which cause low energy storage density of hybrid PCMs, limit its operational applications in phase-change thermal energy harvesting owing to the limited surface area and narrow basal spacing for capturing the guest materials. On the other hand, MT has inherent ionic channels and can intercalate other cations, thus increasing the basal spacing of the clay, which provides accessibility for capturing organic guest materials (Shen et al. 2025). For example, MT modified with n-octadecylamine demonstrated a 4.5-fold increase in the octadecane encapsulation efficiency and up to 243 J g^{-1} latent heat storage density (Liao et al. 2017). Despite satisfactory improvement in storage capacity, the overall thermal regulation efficiency remains primarily dependent on the inherent thermal conductivity of the composite matrix. While low thermal transport helps retain heat over an extended period, it also limits the dynamic response of solid–liquid phase transition systems, which are regulated by the energy materials and hybrid scaffolds. Therefore, the engineering of mineral-based frameworks and their further integration with functional materials, such as biochar, are of considerable practical importance for thermal management applications (e.g., building energy efficiency), an area that remains underexplored. Additionally, considering the diverse structural functionality of biochar together with the potential of engineered biochar in guest materials adsorption and thermal transport, we believe that combining biochar and mineral clays could provide synergistic benefits to composite systems–particularly in terms of encapsulation capacity, phase change thermal energy storage, sustainability, and advancing practical thermal management applications, as demonstrated in an MT-induced cellulose/biochar composite which exhibited reduced degradation rate (44.5%) and improved strength (30.9%) (Kassem et al. 2022). To the best of our knowledge, no prior studies have focused on utilizing engineered mineral-doped biochar, a "green-of-green hybrid" for phase change thermal regulation systems.

In this study, we developed a liquid paraffin-infused biomineral-based composite material to realize high energy storage capacity, desirable thermal transport properties, and reliability via a sustainable and cost-effective method. Typically, low-cost and naturally sourced MT is integrated with biochar, with the resultant hybrid material employed as a support for liquid paraffin. The mineral was engineered with a water-assisted surfactant, cetyltrimethylammonium bromide (CTAB), followed by the introduction of spruce tree-derived carboxy biochar (SB) to yield a structurally distinctive biomineral that exhibited high paraffin adsorption, superior latent heat storage, and satisfactory thermal insulation compared to the bulk MT-based composite, owing to its large specific surface area. The intercalated MT provides increased interlayer spacing, which can be used to reduce the strong interaction of biochar with PCMs, thus highlighting its remarkable encapsulation efficiency and ensuring exceptional stability. Furthermore, this study provides a promising path for fabricating next-generation renewable energy materials with outstanding thermal performance, potential applications in building finishing materials, and low costs.

2 Materials and methods

2.1 Materials

Naturally available MT mineral with 8–12% moisture, 0.75–0.85 g cm^{-3} bulk density, and over 80% particle size (200 mesh pass) was obtained from Ilsung Chemical Co., Ltd., South Korea. SB was obtained from PEFC-certified spruce feedstock carbonized at 600 °C (Carbofex Oy, Finland). n-Hexane (produced by SASOL Germany), used as an energy storage material, was purchased from Celsius Korea Inc. (Seoul, South Korea).

2.2 Preparation of engineered MT and EMB materials

The proximate characteristics, including ash and fixed carbon contents of biochar are provided in supplementary materials (Table S1). The modification of MT and integration with a biochar (EMB) sample is shown in Fig. 1. MT was modified with CTAB following a previously reported method (Batra et al. 2021) with some modifications. Approximately 5 g of MT was introduced into 100 ml of distilled water with continuous stirring and

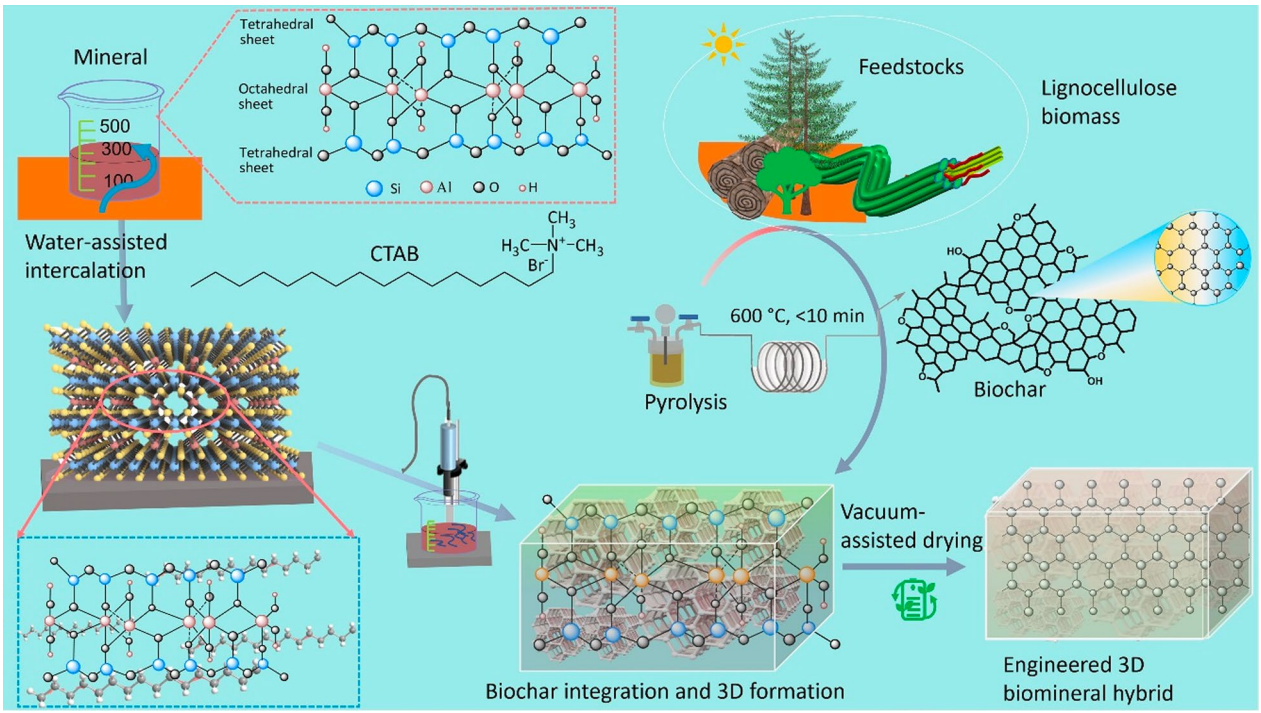

Fig. 1 Schematic illustration of engineered biomineral preparation using modified mineral

ultrasonicated using a VCX-500 ultrasonicator (SONICS, USA) for 30 min at 22–25 °C. Subsequently, CTAB (3 g) was dispersed in the suspension and ultrasonicated for 5 h at a frequency of 20 kHz and 50% amplitude (power of ~ 250 W) under 20 s pulse mode. The matrix was then sieved and washed several times until the water became clear, separated to obtain modified MT (EMT), and subjected to drying overnight (~ 16 h) at 80 °C in a vacuum drying oven at 0.1 kPa. Subsequently, a mixture of EMT and SB in a 1:3 wt.% ratio (EMT to biochar) was dispersed in distilled water and ultrasonicated for 2 h to produce EMB. The dried sample was then used to infuse liquid hexadecane.

2.3 Preparation of EMB@C_{16} composites

EMBP composites were developed using the vacuum encapsulation technique. First, 4 g of EMP was placed in a glass tube and subsequently mixed with liquid hexadecane (8 g) under continuous stirring to ensure a homogeneous PCM infusion. The mixture was then positioned in a vacuum oven at 70 °C overnight. The extra liquid hexadecane was filtered and separated to obtain the thermally stored EMB@C_{16} composite. The obtained solid mixture was dried at 70 °C for 24 h under vacuum. For comparison, SB@C_{16} and EMT@C_{16} were fabricated using similar synthesis processes. Figure 1 presents schematics of thermal storage biomineral-based composites.

2.4 Characterizations of PCM carriers and mineral-doped biochar-based composites

The microstructures of the EMT and SB and the interface morphology of the EMB and hybrid PCMs were observed using field-emission scanning electron microscopy (FE-SEM, JSM-7800F, JEOL Ltd., equipped with EDS elemental mapping capability). Fourier transform infrared (FTIR) spectroscopy was used for evaluating the functional groups over the 4000–500 cm^{-1} range. The chemical compositions and elemental binding energies of EMT, SB, and EMB were determined using X-ray photoelectron spectroscopy (XPS, Thermo VG, U.K.) with an X-ray power of 12 kV and 3 mA. The thermal conductivity of the as-prepared samples was calculated from the thermal diffusivity measured using a NETZSCH LFA 717 (LFA Xenon Flash Lamp). The X-ray diffraction patterns of EMT, SB, and MT without modification (MTB) measurement were conducted with a Cu–K (λ = 1.541 Å) radiation source and LYNXEYE XE detector from 5° to 90° at a scanning rate of 10° min^{-1}. The thermal and shape stability of the sample materials were investigated using thermogravimetric analysis (TGA; Q5000, TA Instruments) under an N_2 atmosphere and by placing the sample above the melting point of C_{16} (80 °C), respectively. The phase transition enthalpy and phase transition temperature of hexadecane, EMB@C_{16}, EMT@C_{16}, and SB@C_{16} were measured using differential scanning calorimetry (DSC;

TA Instruments) from − 5 °C to 50 °C at a scanning rate of 10 °C min^{-1}. Moreover, the durability and thermal management performance of as-synthesized samples were evaluated using a thermal cycler for 1000 heating–cooling cycles and thermal infrared imaging, respectively. The N_2 adsorption and desorption isotherms of MT, EMT, SB, and EMB were recorded at 77 K using a Quantachrome Autosorb-iQ3 Brunauer–Emmett–Teller (BET) analyzer. The surface areas and pore size distribution of the SB and EMB were investigated via the BET model by fitting gas adsorption points in the 0.05–0.3 bar pressure range and the DFT model from gas adsorption isotherms, respectively. The energy-saving performance of the biomineral-based phase change composite and bulk sample was confirmed using DesignBuilder simulation based on the ASHRAE standard 90.1 prototype building model.

3 Results and discussion

3.1 Structural properties of bio-clay mineral scaffolds

The biochar was integrated with organic CTAB modified clay mineral to improve cationic interaction, as illustrated in Fig. 2a. The microstructures of MT, EMT, EMB, and SB were observed using SEM, and they exhibited ordered and vascular structural morphologies in the biochar samples (Fig. 2b). As presented in Fig. 2c and d, the surface morphologies of MT and EMT were aggregated. After modification with CTAB, the surface morphology of the biomineral changed to a smooth surface with aggregations caused by the hydrophobic nature of the clay mineral surface, further signifying surface modification with the alkyl carbon chain and $-NH_2$ of CTAB. Thus, modified MT was doped onto the biochar in the form of scales, as shown in Fig. 2e. This combination subsequently created a good morphology without significantly impacting the biochar microstructure, which is essential for advancing the thermal performance of phase-change composites. The EDS spectra confirm that the main elements are Al, Si, O, and C (Fig. 2f). The elemental distribution of EMB demonstrates that C content (3.48 wt.%) is densely concentrated after SB loading with reduced Si and Al—common for nanopore composites in two sizes (Qiu et al. 2025), thus indicating an effective combination of MT and SB.

However, the effects of MT modification on biochar integration and microstructure have not yet been explored. Therefore, MT without modification, MTB, was prepared to explore the microstructure, the interaction between MT and biochar, and PCM adsorption, and to clarify the influence of energy storage density on biomineral-based composites. As shown in Fig. 2f, the combination of bulk MT with biochar significantly degraded the morphology, microstructure, and interconnected pore network of the biochar, wherein the layer structures almost completely collapsed, presumably due to the comparatively high hydrophilic nature of bulk MT (anionic) (compared with modified MT), which causes structural disruption during polar solvent-assisted ultrasonication of the biochar sample. Acidic minerals, including mineral acids such as H_2SO_4 and H_3PO_4, partially interrupt the fibrous, rigid structure of lignocellulose-based materials, shifting the surface area and morphological features of biochar materials. For example, forestry wood waste-derived biochar interacted with acidic sulfonate showing morphology collapse and demonstrated reduced surface area from 131.9 $m^2\ g^{-1}$ of raw biochar to 59 $m^2\ g^{-1}$ after interaction with anionic compound, whereas pore volume decreased from 0.066 to 0.036 $cm^3\ g^{-1}$ (Xiong et al. 2018). Such a morphological collapse results in an agglomerated block-like morphology that causes difficulty in the phase change process during operation, insufficient guest molecule adsorption, and low energy storage capacity. However, the co-pyrolyzation of biochar with montmorillonite enhances the structural properties, including the surface area and pore volume of the biochar (Yang et al. 2025), wherein corn straw co-pyrolysis with MT improved the porosity and surface area of pristine biochar from 27.0 $m^2\ g^{-1}$ to 53 $m^2\ g^{-1}$, and MT acts as a solid acidic catalyst. However, as observed in the rice straw biochar-MT composite, it still has a lower surface area even in hydrothermally co-pyrolyzed biochar with bulk MT, possibly due to the mutual coverage between the biochar and clay minerals (Yuan et al. 2024).

To further explore the structural properties and interactions between clay minerals and biochar, FTIR analysis was conducted, as presented in Fig. 2g and h. The prominent and characteristic absorption peaks located at 3436, 1630, and 1029 cm^{-1} in pristine MT are attributed to the asymmetric and symmetric stretching of water and Si–O bending vibrations within the MT interlayer, respectively (Atinafu et al. 2021). Meanwhile, a slight blue-shift occurred for EMT at the –OH stretching vibration of 3435 cm^{-1} and the Si–O bending vibration at 1027 cm^{-1} showing a slight reduction in intensity compared with bulk MT, thereby signifying that the hydrophobicity of EMT is improved because of the intercalation of organic CTAB cations. Notably, the distinct absorption peaks at 2923 and 2853 cm^{-1} after organic modification were associated with the stretching vibrations of the $-CH_3$ and $-CH_2$ alkyl groups of EMT, suggesting that CTAB induced alkyl groups in the clay minerals (Fig. 2h1). Additionally, the faint absorption peak at 1423 cm^{-1} is attributed to the bending vibrations of the C–H of the $-CH_3$ group of the amine groups, demonstrating the introduction of cationic CTAB into the clay mineral (Liu et al. 2022; Yang et al. 2023). However, the asymmetric

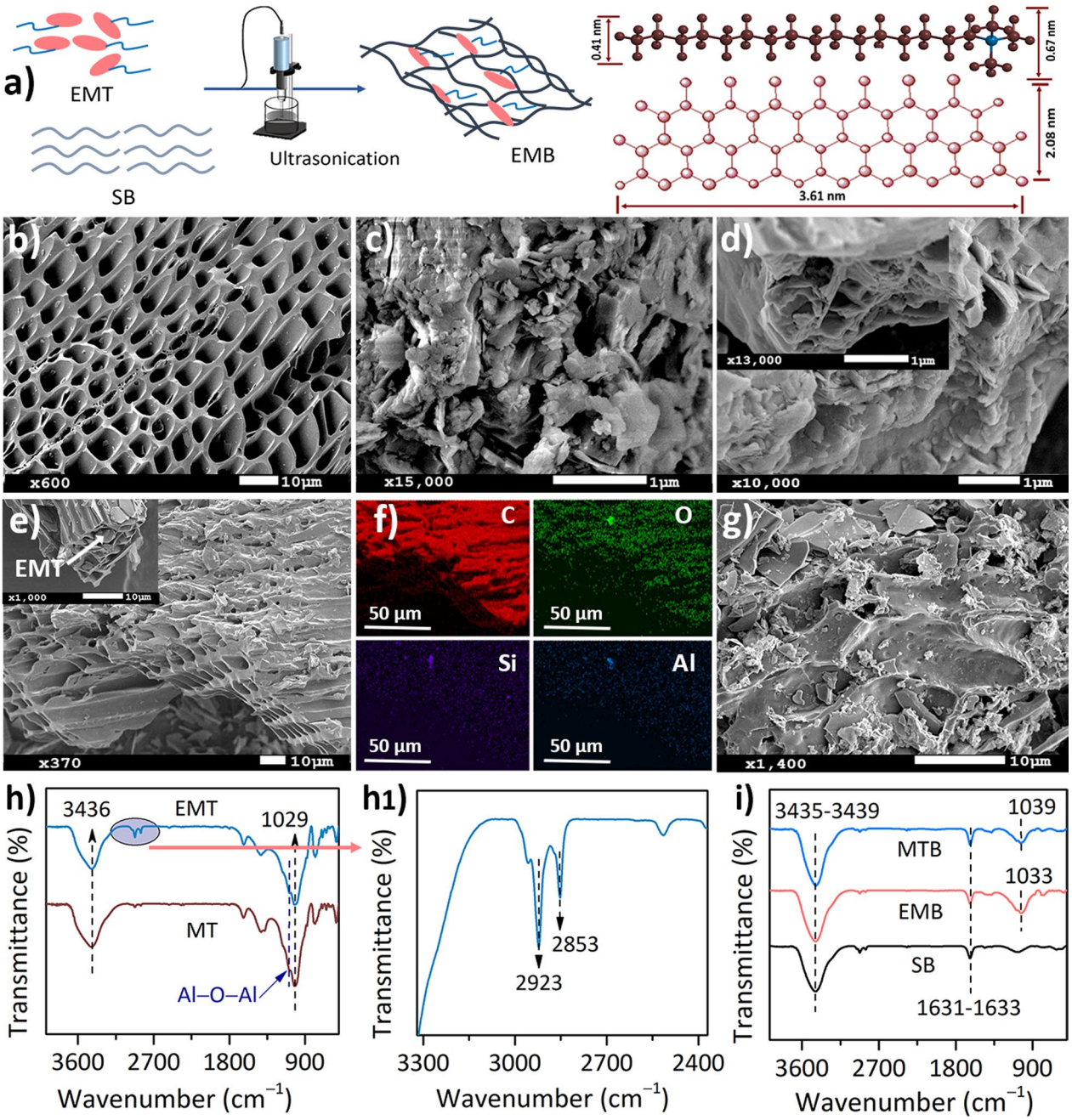

Fig. 2 Structural and morphological properties of biochar, engineered biomineral, and clay mineral samples. **a** Schematic illustration of EMB biomineral fabricated using ultrasonication with water as the solvent. The right shows the molecular conformation of CTAB (top) and the planform view of MT (bottom). SEM images of (**b**) SB, (**c**) MT, (**d**) EMT, (**e**) EMB, (**f**) EDS elemental spectra of Al, C, Si, and O, and (**g**) MTB. FTIR spectra of (**h**, **h1**) MT, EMT, and (**i**) high-resolution FTIR spectra of EMT from 3320 to 2370 cm.$^{-1}$

peak intensities and positions of Al–O–Al (1083 cm^{-1}, overlapping with strong Si–O peaks) and Si–O showed no obvious changes after organic modification, indicating that the intercalation of CTAB has insignificant influence on the main structure of the bulk MT layers. In the spectra of biochar-induced biomineral hybrids, EMB and MTB showed typical bands in the range of 3435–3439 cm^{-1} associated with –OH stretching vibrations, and the peaks at 1631–1633 cm^{-1} come from C=O/C=C absorption peaks of the SB structure, becoming stronger in biomineral samples compared with the pristine EMT. The Si–O bending vibrations of MTB showed a blue shift

at 1039 cm^{-1} after biochar integration, presumably due to the strong interaction between MT and SB as well as the change in structural morphology, as depicted in the SEM image in Fig. 2g. The rate of change of the stretching peaks of EMB at 3437 cm^{-1} (–OH) and 1033 cm^{-1} (Si–O) and the shifts from EMT suggest the reinforcement of hydrogen bonds with SB. The –OH groups in the biochar also preferentially changed because the active hydroxyl groups in the mineral and biochar can form numerous hydrogen bonds, which dramatically shift the absorption peak of the hydroxyl groups (Kang et al. 2025).

The crystallinity of the biomineral materials was characterized using XRD. EMB combined the diffraction patterns of pristine MT and biochar with the main mineral component silica and diffraction peaks of 2θ = 20.9° (100), 26.7° (101), 36.6° (110), 39.5° (012), 50.2° (11–2), 59.9° (21–1), and 68.2° (023) (Fig. 3a). For SB, the peaks were broad with standard Bragg reflections (002) peaks at 2θ = 22.9° and (100) at 43.5°, suggesting the amorphous characteristics defined by a low degree of "graphitic carbon" structure—advantageous for enabling thermal transport and improving energy conversion properties (Li et al. 2025). Notably, after intercalation and assembly with SB, the peak intensity of MT was reduced and even disappeared for the peaks at 2θ = 8.9° (d = 9.9 Å) crystal spacing. Besides the crystallinity and morphological

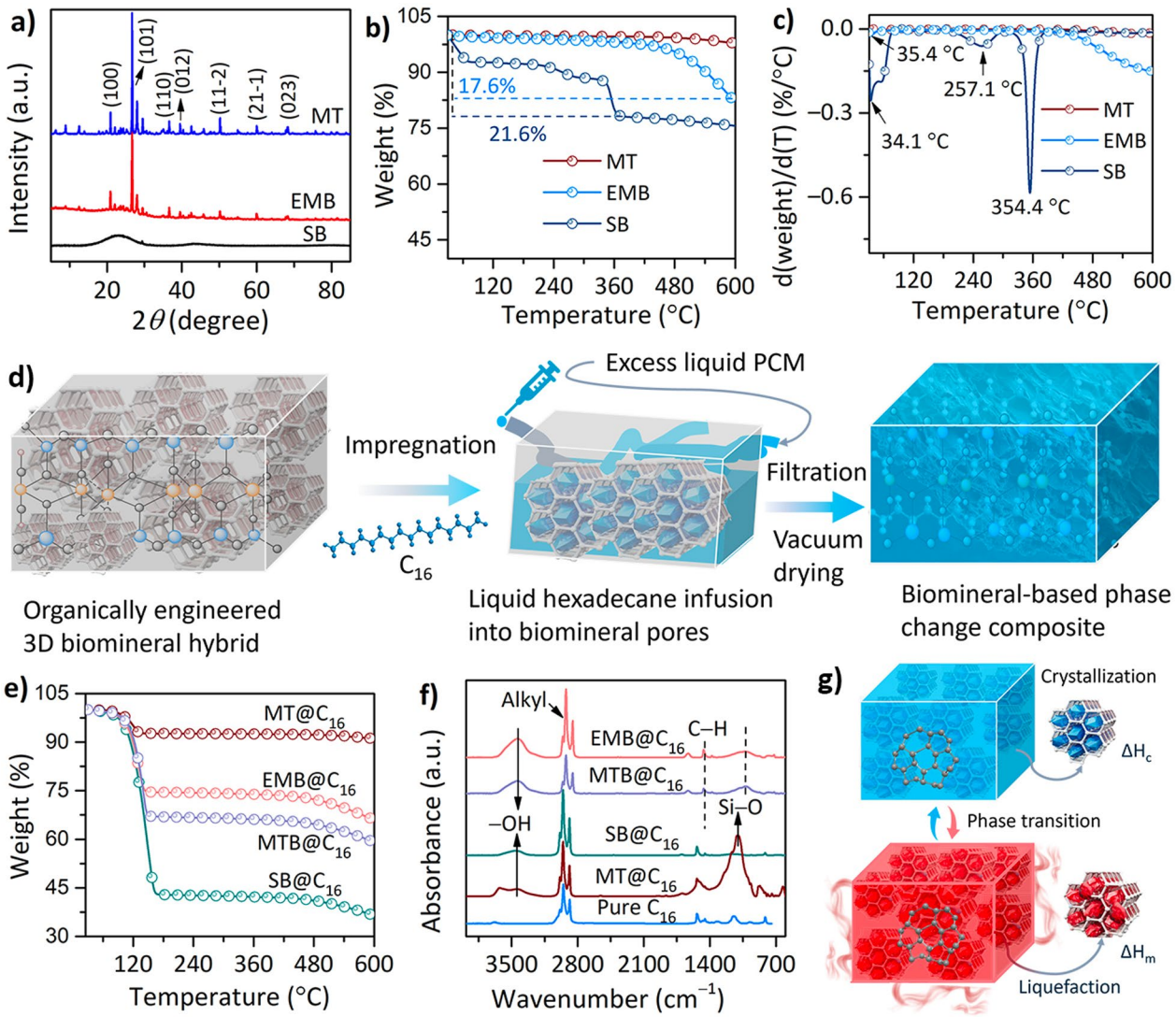

Fig. 3 Structural and thermal stability performance of biominerals, clay minerals, and composite materials. **a** XRD patterns, (**b**, **c**) TGA curves and corresponding DTG thermograms of supporting scaffolds. **d** Illustration of biomineral-based paraffin composite. **e** TGA curves and (**f**) FTIR spectra of paraffin-based composite materials. **g** Schematic descriptions of phase transition during the energy-saving and energy-releasing process

characteristics of PCM scaffolds, the degradation in performance owing to weight is crucial when fabricating phase change composites, and the TGA measurements are presented in Fig. 3b. The bulk MT and EMB maintained structural integrity with negligible weight reduction up to 450 °C for EMB and approximately up to 600 °C for MT, indicating their potential capability in PCM support. In contrast, SB demonstrated slightly lower thermal stability with a maximum weight degradation that occurred at 354.4 °C (Fig. 3c) owing to the decomposition of organic compounds (such as lignin) and at lower temperatures (34.1 °C) following the elimination of scums including moisture from the biochar framework—a property analogous to the moisture content of SB (30–50%). The high thermal stability of MT and EMB renders them promising carriers for PCM adsorption, as illustrated in Fig. 3d, benefiting from the synergistic structural properties of MT and biochar and enhancing the seepage resistance while retaining suitable heat transfer performance. Therefore, the paraffin-based composites exhibited high thermal stability (Fig. 3e), with weight loss occurring between 120 and 160 °C with a weight degradation of 57.1, 25.5, and 7.3 wt.% associated with the decomposition of C_{16} in SB@C_{16}, EMB@C_{16}, and MT@C_{16}, respectively, as organic PCMs decomposed from 120 to 250 °C (Zhu et al. 2025). In addition, the composite revealed complete decomposition until approximately 450–475 °C and showed slight residual loss of 4.7, 6.8, and 1.2 wt% for SB@C_{16}, EMB@C_{16}, and MT@C_{16}, respectively, presumably due to the decomposition of supporting materials, as observed in the corresponding individual materials.

To confirm the effective fabrication of the composite materials, FTIR spectroscopy was performed (Fig. 3f), where clay mineral-integrated composites demonstrated broad absorption bands at 1014, 1032, and 1028 cm^{-1} for MT@C_{16}, EMB@C_{16}, and MTB@C_{16}, respectively, associated with the antisymmetric stretching vibration peak of Si–O in the clay minerals. However, the absorption peak intensity was much higher in MT@C_{16} than in the other two composite materials because of the biochar interference in MTB@C_{16} and EMB@@C_{16} and the intercalation of organic materials in the EMB. All the composites exhibited stretching vibration peaks in the range 2923–2924 and 2853–2854 cm^{-1}, attributed to the C–H bonds of $–CH_3$ and $–CH_2$ groups, where EMB@C_{16} preserved the stretching vibrations of pristine C_{16} exhibited at 2983 and 2853 cm^{-1}, which is used to enhance the energy storage capacity due to easy molecular chain movement during the phase transition process, as shown in Fig. 3g (Gao et al. 2018). Meanwhile, SB@C_{16} revealed the characteristic peaks of biochar and C_{16}.

However, the composite materials, particularly those fabricated using EMB and MTB, exhibited markedly attenuated Al–O and Si–O stretching peak intensities relative to their corresponding pristine counterparts, implying the formation of hydrogen bonding interactions. Hydrogen bonding is a pervasive non-covalent intermolecular interaction characterized by relatively low bond dissociation energies, typically ranging from 5 to 20 kJ mol^{-1} (Yu et al. 2024). Hence, the abundant hydrogen bonding between the inter- and intramolecular chains is presumed to act as an internal stress reservoir, contributing to the preservation of the elongation conformation of the molecular chains in the absence of external forces (Geng et al. 2024).

XPS was employed to evaluate the surface valence states and binding energies of the biomineral and SB. The survey spectra of the EMB revealed the occurrence and relative contents of C and O at binding energies of 283.6 and 531.9 eV (Fig. 4a). The new peaks in the EMB associated with Si 2p (102.6 eV) and Al 2p (74.1 eV) (Fig. 4a, inset)—absent in the SB spectrum—further confirm the integration of clay minerals with biochar, consistent with the FTIR results. The high-resolution C 1 s signal of EMB confirm the existence of three major peaks at 283.6, 284.3, and 286.5 eV associated to C–C/C=C, C–O, C=O, respectively (Fig. 4b). Meanwhile, SB matched the peak characteristics with a slight increase in the corresponding binding energies of carbon (Fig. 4c), indicating that the C species presumably bonded/interacted with other species, such as nitrogen, from CTAB, and metallic species in EMB, resulting in the formation of C–N that can mostly overlap with C=C (Li et al. 2024). Furthermore, the intensity of the deconvoluted O 1 s of EMB (Fig. 4d) was observed to be much lower than that of the SB O 1 s (Fig. 4e), signifying a higher interaction of electrons in the EMB, resulting in the formation of coordinated orbitals used to improve the thermal transport.

Furthermore, the SEM characterization confirmed the open pores in the biochar, SB, MT (average pore diameter of 12.65 nm), and biominerals (MTB and EMB) with the average pore diameter measuring 4.16–4.65 nm, which allowed the C_{16}, a PCM, to be absorbed and impregnated within the pore structure of the hybrid layers (Fig. 5a–d) while maintaining the liquid flow of pristine hexadecane under phase transition temperatures. The pores of all the materials were completely occupied by the PCMs, leaving no vacant space. Indeed, the EMB effectively impregnated the PCM and exhibited reduced pores without significantly altering the microstructure, yielding composite materials with similar macroscopic morphologies (Fig. 5c). However, the biomineral obtained through mixing and without modification (conventional route), MTB, was subtle to the PCM absorption, resulting in diminished morphology and structure after the vacuum impregnation process and drying above

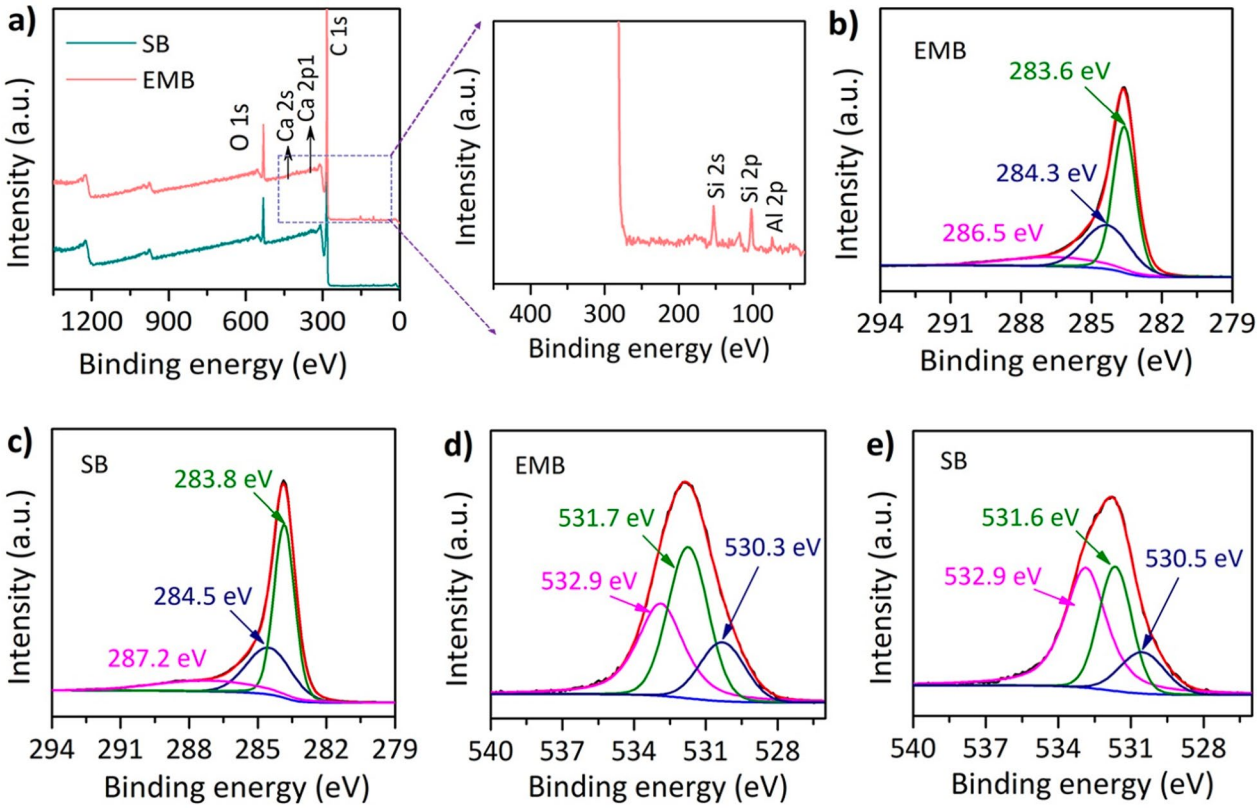

Fig. 4 Surface valence states and binding energy of biomineral and biochar. **a** XPS survey, and high resolution (**b**, **c**) C 1 s and (**d**, **e**) O 1 s spectra

the fusion temperature of C_{16} (Fig. 5d), because of the weak interlayer interactions, including π–π stacking. During mixing and drying, eliminating the solvent from the pores can result in a low degree of crystallinity and reduced surface area. This effect originates from the capillary forces induced by the hydrothermal process and mechanical forces, including evaporation within the pore confinement, which eventually lead to structural deformation and pore collapse (Xue et al. 2025), as illustrated in Fig. 5e. According to the N_2 sorption measurements at 77 K (Fig. 5f), EMB exhibited the highest pore volume (0.0710 $cm^3\ g^{-1}$) and BET surface area (61.02 $m^2\ g^{-1}$), an approximately 516.4% increase compared to the bulk MT (9.9 $m^2\ g^{-1}$) and approximately 23.7% improvement over MTB (49.38 $m^2\ g^{-1}$). The BET specific surface area of EMB was slightly larger than previously reported for MT-boron nitride hybrid materials (52.9 $m^2\ g^{-1}$) (Atinafu et al. 2021) and competitive with that of pyrolyzed (at 500 °C) rice husk biochar-MT hybrid (99 $m^2\ g^{-1}$) (Arif et al. 2023), highlighting its promising potential for phase transition thermal energy harvesting applications. MTB had a lower pore volume (0.0514 $cm^3\ g^{-1}$) and BET surface area (49.38 $m^2\ g^{-1}$). These observations can be rationalized by the structural damage that could lead to insufficient PCM adsorption, ultimately resulting in a low energy harvesting capability of the paraffin-based phase-change composite. Simultaneously, the small initial N_2 uptake ($P/P_o < 0.01$, as shown in the inset of Fig. 5f) is ascribed to the micropores and hysteresis at a high relative pressure ($P/P_o > 0.6$) owing to the mesopore size distribution, as presented in Fig. 4g, where MT shows a mesopore volume centered at a pore diameter of 3.82 nm and both MTB and EMB are at 3.41 nm, largely scattered in the range of 3–15 nm, providing an ideal space for absorbing C_{16} and facilitating thermal transport.

3.2 Thermal performance of biomineral-based paraffin composite

The heat endothermic/exothermic properties of pristine C_{16} (with hexadecane as the PCM), SB@C_{16}, MT@C_{16}, and biomineral-based MTB@C_{16} and EMB@C_{16} were evaluated using DSC. As presented in Fig. 6a and b, all the composite materials exhibited approximately similar trends for endothermic and exothermic peaks as C_{16} during the crystallization and liquefaction processes, indicating that the supporting scaffolds did not affect the phase transition characteristics of C_{16}. The corresponding melting and crystallizing latent heat (ΔH_m and ΔH_c), melting

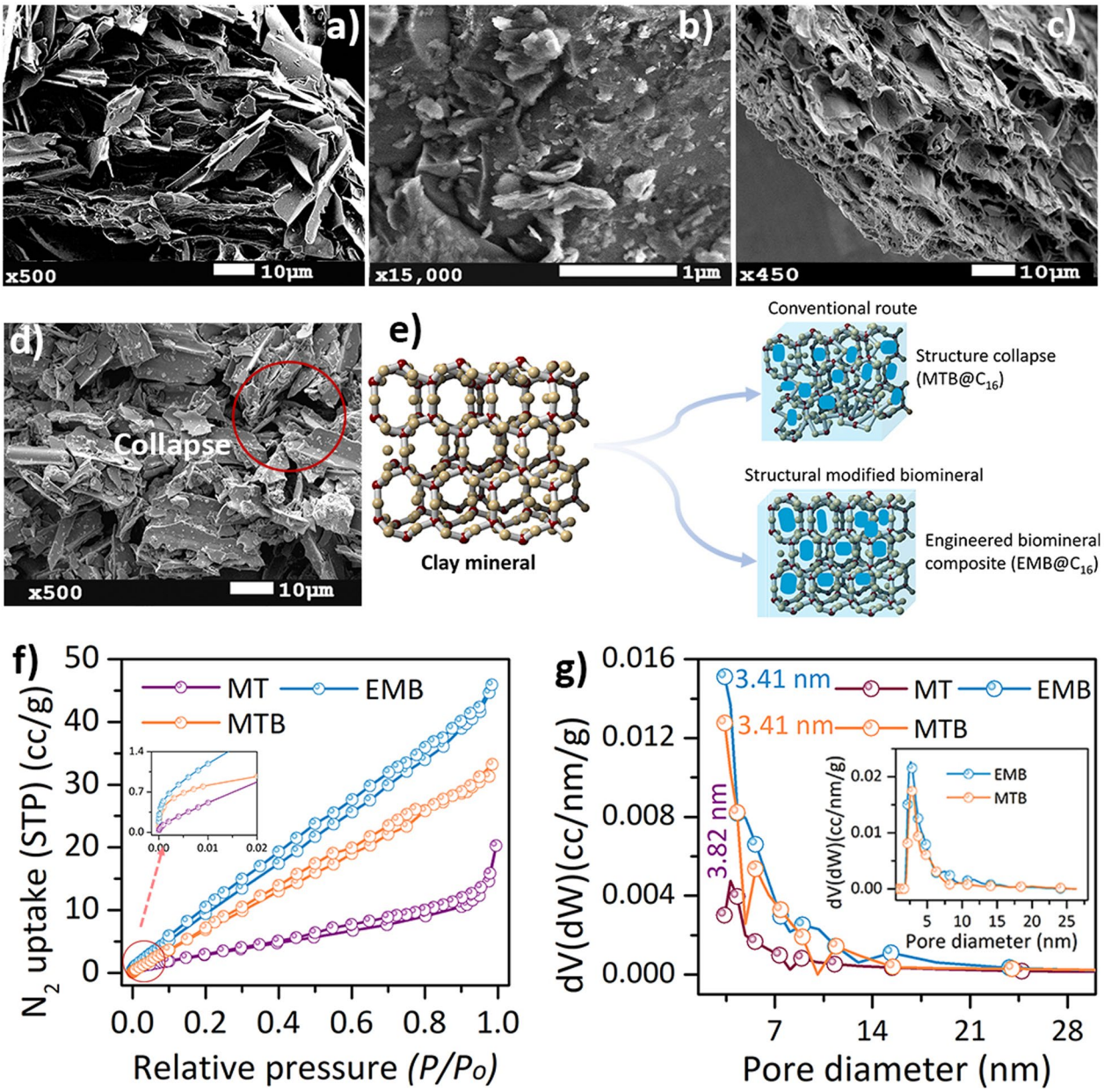

Fig. 5 Microstructure of biomineral composite materials and organically modified clay minerals. SEM images of (**a**) SB@C16, (**b**) MT@C_{16}, (**c**) EMB@C_{16}, and (**d**) MTB@C_{16}. **e** Schematic illustration showing biomineral-based phase- change composite by conventional route and organically engineered biomineral-based phase- change composite. **f** N_2 uptake isotherms and (**g**) BJH pore size distribution of MT, MTB, and EMB. Inset is the DFT pore size distributions of biominerals

temperature (T_m), and crystallizing temperature (T_c) of the as-prepared materials were computed using the integral areas under the endothermic and exothermic peaks, as presented in Fig. 6a–c. T_m, T_c, and ΔH_m and ΔH_c for C_{16} were found to be 21.7 °C, 10.9 °C, 185.8 J g^{-1}, and 185.3 J g^{-1}, respectively. For the composite materials, T_m and T_c were observed to be in the ranges of 19.1–23.7 °C and 9.3–11.6 °C, respectively, while the corresponding ΔH_m and ΔH_c values ranged from 15.7 to 121.3 J g^{-1} and from 15.3 to 119.9 J g^{-1}, respectively. These results indicate that the thermophysical properties of C_{16} are maintained in the enclosures surrounding or encapsulating the PCMs, enabling efficient phase-transition performance. The decrease in the enthalpy of the composite materials, relative to the pristine C_{16}, is because the added MT, SB, MTB, and EMB do not undergo phase change, thereby

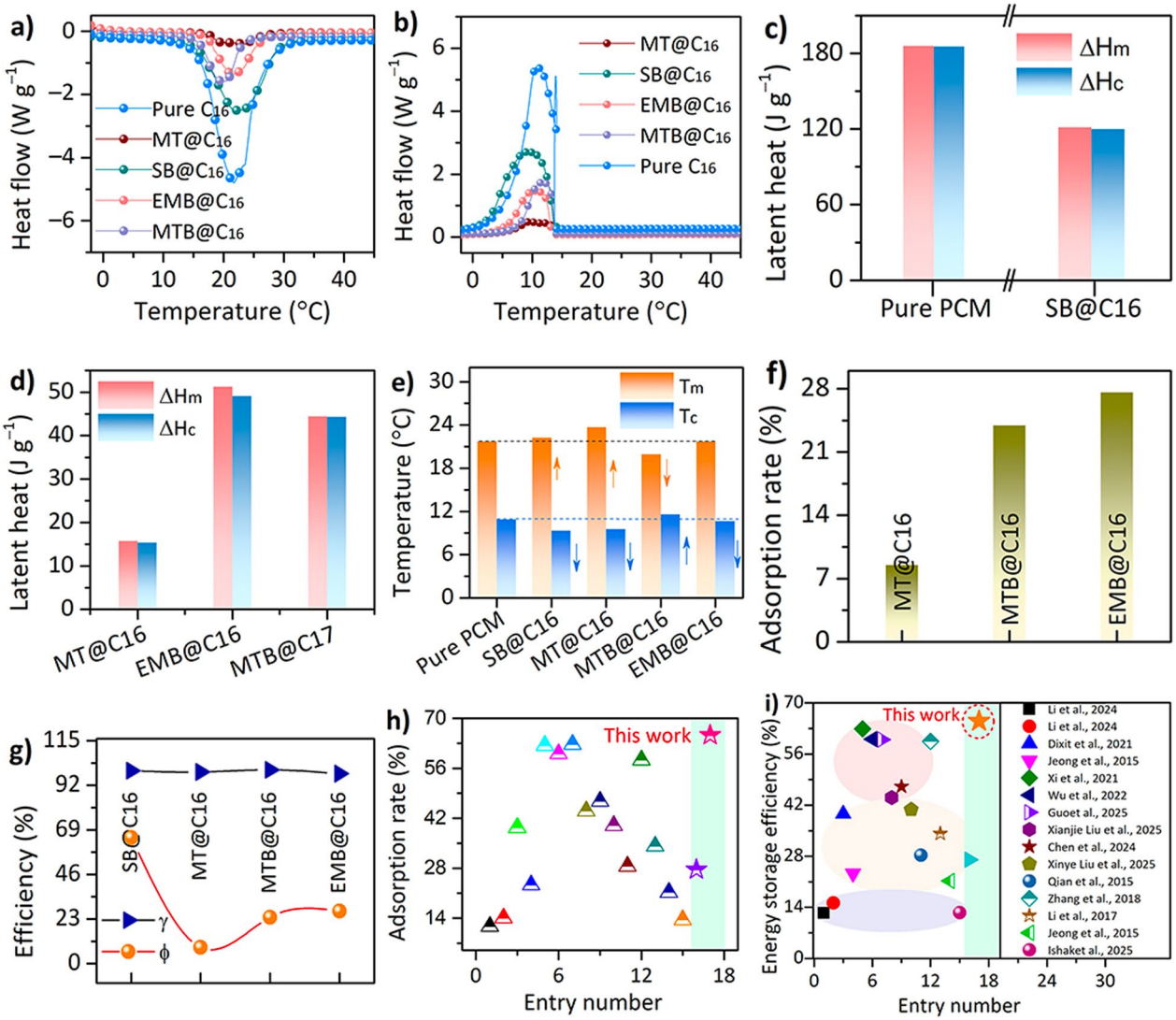

Fig. 6 Phase transition and thermal performance of bulk and biomineral-based phase change composites. DSC curves of (**a**) exothermic and (**b**) endothermic thermograms. **c** Latent heat storage of pure hexadecane and SB@C_{16}, **d** melting-crystalline enthalpy of biomineral-based phase change composites and clay mineral-based composite materials, **e** phase-transition temperature, **f** PCM adsorption rate of composites, and **g** relative latent heat retention and encapsulation efficiency of phase change composite materials. Comparison of (**h**) adsorption rate and (**i**) energy storage efficiency of biomineral-based PCMs and reported mineral-based composites

confining and restricting the normal phase change behavior and reducing the weight fraction of C_{16} within the composites. However, the energy harvesting capabilities of the biochar- and biomineral-based composites were significantly higher than those of bulk MT-based composite MT@C_{16}. Specifically, EMB@C_{16} and SB@C_{16} demonstrated enhancements of approximately 223.3% and 670.6%, respectively, which can be ascribed to the improvement in the specific surface area (an increase of 516.4% from bulk MT) achieved by employing modified mineral-doped biochar. The high PCM content in the EMB and SB played a major role in defining the amount of excess thermal energy that could be absorbed by a given volume.

Additionally, the interfacial interactions—comprising capillary forces, surface polarity influences, and hydrogen bonding—that arise between C_{16} and scaffolds play a significant role in the crystallinity of PCM and latent heat storage density (Li et al. 2013). Thus, the proportion of ΔH_m in the biochar and biomineral-based samples, referred to as absorption rate (ϕ), is used to approximate the PCM content. It can be calculated using the formula $\phi = \Delta H_{m.composite}/\Delta H_{m.C16}$, where $\Delta H_{m.composite}$ and $\Delta H_{m.C16}$ are the melting enthalpies of the composite and bulk

C_{16}, respectively, and their values ranged from 23.9% to 70% of the value for pristine hexadecane (Fig. 6f and g). The energy storage efficiencies of EMB@C_{16} and SB@C_{16}, expressed as relative heat retention (γ), were 98% to 99.6% (Fig. 6g), indicating that most of the PCM absorbed in the supporting materials was effectively utilized in the phase-change thermal energy performance, with a few PCMs potentially constrained by intermolecular interactions and confinement, impeding complete phase transition and utilization (Lee et al. 2024). In this regard, the surface polarity of EMB was notably lower than that of the bulk counterparts with C_{16}, as it was engineered using CTAB and introduced the nonpolar alkyl functional group on its surface. This resulted in reduced interaction between C_{16} and EMB and showed high crystallinity, defined as the ratio of $\Delta H_{m.composite}$ to the product of $\Delta H_{m.C16}$ and its loading in the composite, close to 1 (0.98). In contrast, in MT@C_{16}, some C_{16} molecules are adsorbed in pores of the MT, where they experience stronger capillary confinement and polar surface interactions, including hydrogen bonding. These combined interactions hinder the mobility and solidification of C_{16}, leading to lower crystallinity and reduced latent heat. Furthermore, the BET surface area and pore volume of biominerals were used to uncover the mechanism for enhanced ϕ and γ of biomineral-based composites. As indicated earlier, EMB exhibits a significantly higher surface area (61.02 $m^2\ g^{-1}$) and pore volume (0.0710 $cm^3\ g^{-1}$) compared to MT (9.9 $m^2\ g^{-1}$ and 0.0313 $cm^3\ g^{-1}$, respectively). This implies that engineered biochar-based material has greater adsorption capacity than the bulk material, which may be because the PCM molecular chains are allowed more freedom to move and crystallize, leading to the higher crystallinity of hexadecane in EMB@C_{16} and thus an enhanced latent heat capacity. Additionally, the energy storage density of the developed composite materials is highly competitive and even higher than that of recently documented mineral-based hybrid composites (Fig. 6h and i, Table 1).

3.3 Long-term stability of biomineral-based composite materials

The chemical and thermal cycling durability performance of the composite materials was evaluated after subjecting the samples to 1000 heating–cooling cycles, from ambient temperature (23 °C) to 50 °C, using an accelerated thermal cycler. As presented in Fig. 7a, the composite materials exhibit phase-change peaks similar to those of the composite before 100 cycles, aligned with those of

Table 1 Thermal performance of as-prepared biomineral-based PCMs with some previously reported mineral-based and conventional biochar-based composite materials

Entry	Composite	Pure PCM latent heat storage	Phase transition temperature	Latent heat storage	*K* enhancement (%)	Reference
		$\Delta H_m/\Delta H_c$ (J g^{-1})	T_m/T_c (°C)	$\Delta H_m/\Delta H_c$ (J g^{-1})		
1	BGC@C_{14}	228.3/228.2	33.8/24.8	30.2/26.7	–	(Li et al. 2024)
2	BGC@C_{18}	245.9/245.8	56.4/50.3	40.2/34.5	1.2	(Li et al. 2024)
3	Propyl palmitate/expanded perlite	149.94/147.8	18.6/15.4	59.0/58.9	–	(Dixit et al. 2021)
4	n-hexadecane/Na-MMT	254.7/–	18.65/14.56	61.4/59.3	214.3	(Jeong et al. 2015)
5	P25/RGO@PW	176.7/171.9	55.9/47.6	110.2/109.1	168.6	(Xi et al. 2021)
6	EPDM/MXene/PW	198.2/189.6	59.1/53.3	119.1/113.9	–	(Wu et al. 2022)
7	KBC1.5/CNT3/MA	192.7/192.2	55.76/47.2	120.8/110	40.1	(Guo et al. 2025)
8	DC4-PA	201.2/198.5	58.9/39.6	88.6/87.5	–	(Liu et al. 2025a, b)
9	PW@35Al	224.7/225.8	60/49.5	105/107.0	4450	(Chen et al. 2024)
10	PA1/F-DE/ZnO_{10} (cycle 1)	197.7/186.1	38.8/35.6	78.99/77.4	87.7	(Liu et al. 2025a, b)
11	PEG/diatomite/Ag	180.3/164.6	59.21/38.63	51.5/46.1	–	(Qian et al. 2015)
12	$CaCl_2{\cdot}2H_2O$/diatomite/paraffin	185.6/161.8	28.9/3.2	108.2/98.5	–	(Zhang et al. 2018)
13	OMMT/paraffin/grafted MWNT	139.5/–	21.5/28	47.7/–	72.9	(Li et al. 2017)
14	n-Octadecane/Na-MMT	247.6/–	31.47/22.13	56.6/54.1	49.6	(Jeong et al. 2015)
15	Expanded perlite/capric acid	164.70/164.5	33.18/10.57	22.3/19.1	–	(Ishak et al. 2025)
16	OH-WCG/paraffin	172.8/172.8	55.1/46.8	84.7/83.1	53.0	(Yin et al. 2024)
17	Biochar/paraffin	184.0/184.1	58.3/55.9	171.9/146.8	15.7	(Lv et al. 2024)
18	CA–MA/VMT/EG	154.8/156.4	19.7/17.1	26.9/–	46.7	(Karaipekli & Sarı, 2009)
19	EMB@C_{16}	185.8/183.3	21.71/10.66	51.2/49.1	78	This work
20	SB@C_{16}	185.8/183.3	22.22/9.31	121.3/119.9		This work

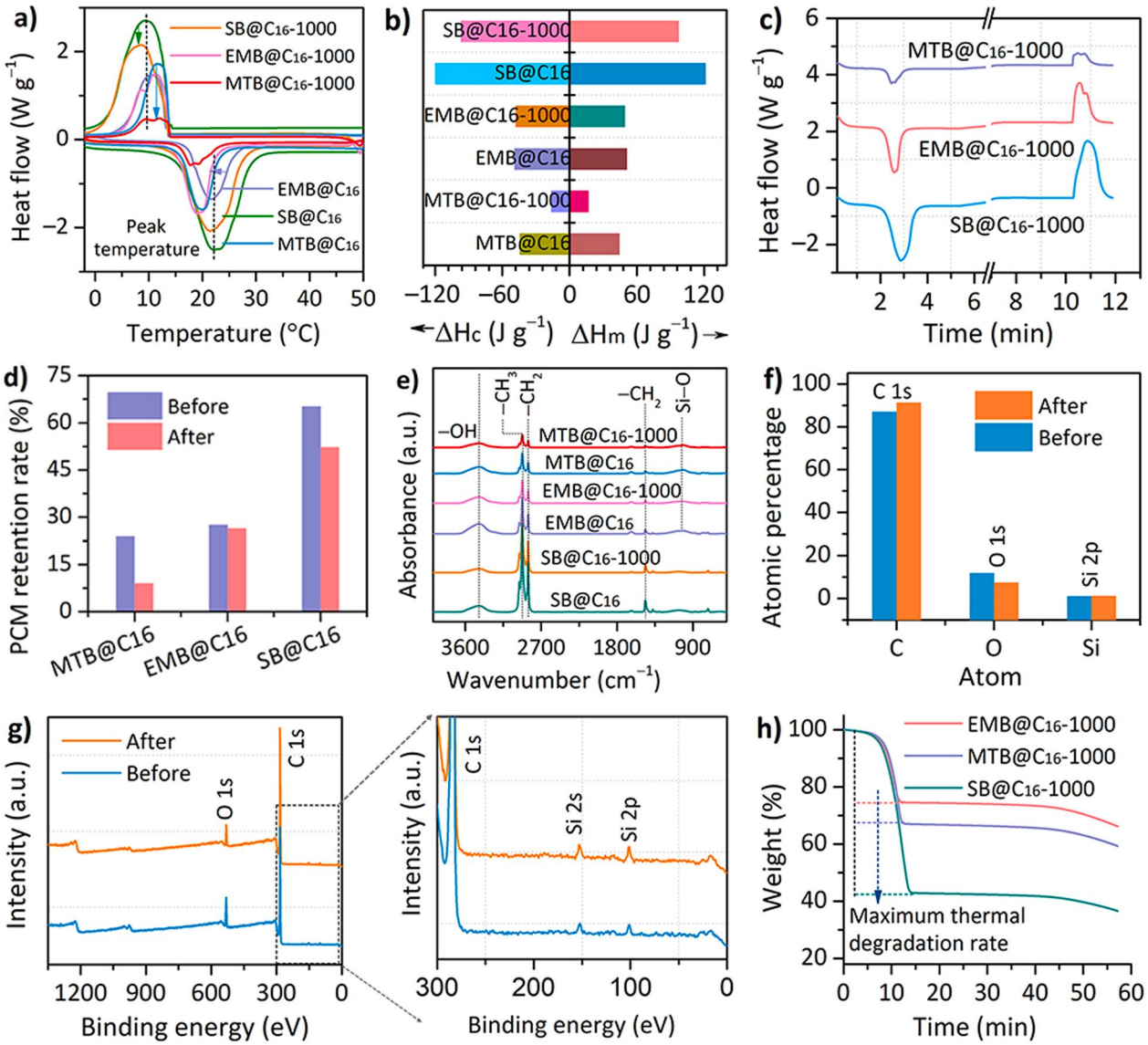

Fig. 7 Long-term phase change thermal storage performance. **a** DSC curves after 1000 heating–cooling cycles of SB@C_{16} and EMB@C_{16}. **b** Thermal energy uptake and release during heating–cooling cycles, **c** Heat flow against time phase transition process. **d** PCM retention potential after 1000 cycling, **e** FTIR analysis of pre- and post-1000 thermal cycles, **f** Atomic percentage of biomineral-based phase change composite after and before cycling, **g** XPS survey of EMB@C_{16} after and before thermal cycling, and (**h**) Thermal degradation against time curves of phase change composites after heating and cooling cycles

pure C_{16} molecules. This further indicates that the C_{16} molecules preserve their melting and freezing properties within the pore structures of SB and EMB. Notably, the biomineral composite PCMs exhibit outstanding thermal energy storage retention capacity with only a slight shift of 4.1%, whereas a 19.8% reduction was observed for SB@C_{16} (Fig. 7b). This is attributed to the strong confinement effect in EMB@C_{16}, which effectively preserves the PCM from leakage in its liquid state, retaining over 95.9% and 80.2% PCM in EMB@C_{16} and SB@C_{16}, respectively, after thermal cycling process involving approximately 15 min of heat flow (Fig. 7c and d). In contrast, MTB@C_{16} (based on unmodified MT-biochar support) demonstrated the lowest phase-transition peak intensity and retained only about 38.0% of its original latent heat after thermal cycling, presumably due to the weak interfacial interactions between the mineral and biochar, making the composite more susceptible to PCM leakage.

Furthermore, FTIR spectral analysis after 1000 cycles confirmed that the prominent absorption peaks

corresponding to the functional groups, such as $-CH_3$ (2923 cm^{-1}), $-CH_2$ (2853 cm^{-1}), and –OH (3435 cm^{-1}) remained unchanged (Fig. 7e), highlighting the high phase composition stability and chemical compatibility between paraffinic hexadecane and biomineral matrices. However, a reduction in peak intensities was observed, including the Si–O stretching vibrations range (1000–1100 cm^{-1}) (G. Wang et al. 2025), which is ascribed to the low Si content (1.4%) where the characteristic peaks of Si–O may also be overshadowed by the stronger absorptions from paraffin and biochar. XPS analysis further confirmed the chemical stability of EMB@C_{16} after thermal cycling. After 1000 cycles, the surface elemental composition showed only minor raw variations: 4.3% in C and 4.4% in O (Fig. 7f). In contrast, both the EMB@C_{16} and EMB@C_{16}-1000 possessed almost identical Si composition with 0.2% raw difference. The XPS survey spectra revealed a major peak of C 1 s (283.7 eV), O 1 s (531.4 eV) and Si 2p (101.4 eV) (Fig. 7g). Interestingly, a slight blueshift in surface C content was observed after cycling, attributed to seepage and movement of the embedded PCM toward the surface induced by repeated thermal expansion and contraction. Correspondingly, the C 1 s binding energy slightly decreased from 283.7 eV before cycling to 283.5 eV after cycling, indicating a subtle alteration in the chemical environment of surface structures. Additionally, the TGA revealed a single-step degradation profile occurring over approximately 60 min of heating (Fig. 7h), further demonstrating outstanding thermal stability following extended thermal cycling. These results highlight the promising long-term chemical and thermal stability of the biomineral-based phase change composite and the potential for durable, high-performance thermal energy storage and management applications.

3.4 Thermal control demonstration of EMB@C_{16}-based composite phase change materials

The thermal management performance of the as-prepared cationic engineered nanoclay-doped biochar encapsulated paraffin placed on a heating plate was demonstrated by the real-time temperature variations in the heating configuration (50 °C), with the room temperature maintained at approximately 23 °C, ensuring continuous thermal energy supply in MT@C_{16}, SB@C_{16}, and EMB@C_{16} (Fig. 8a and b). As presented in the thermal infrared images in Fig. 8a, when heated to 50 ℃, the composite materials MT@C_{16} demonstrated a slightly higher heating rate than SB@C_{16} and EMB@C_{16}. In the initial stage, within 5 min, the composites experienced orange upper surfaces with a sharp increase to ≈47 °C at 60 min. The surfaces of all the samples turned red uniformly between 30 to 60 min heating rate, signifying the increase in temperature distribution at different heating rates. The surfaces subsequently turned orange at 5 min, bluish-purple at 30 min, and deep greenish-purple at subsequent cooling rates. EMB@C_{16} required 120 s to reach 42.5 °C, while the bulk MT-based phase change composite reached 46.4 °C in the same time, thus highlighting the inherent thermal insulation advantages of EMB@C_{16} in various domains. Notably, the color of the biochar-based phase-change composite was uneven during different heating and cooling processes, suggesting that its thermal conductivity (K) performance was the poorest. This observation was further evaluated by considering thermal diffusivity (α, $m^2\ s^{-1}$), using a NETZSCH LFA Xenon Flash Lamp analyzer. K was calculated as $K = \alpha\rho C_p$, where ρ (kg m^{-3}) and C_p are the density and specific heat (J $kg^{-1}\ K^{-1}$) of composite materials, respectively. C_{16}, used as PCM, has a K of only 0.2 W $m^{-1}\ K^{-1}$ (Fig. 8c). After integration with EMB and MT, the K values of EMB@C_{16} and MT@C_{16} enhanced by 78% and 164%, respectively, compared to that of paraffin. This result is even higher than that of a graphene aerogel/lauric acid phase-change composite, which only increases to 0.328 W $m^{-1}\ K^{-1}$ (Tang et al. 2024). This substantial advancement is primarily ascribed to the favorable pore network of EMB and biochar, which exhibits a dominant mesopore size distribution centered at 3.41 nm and broadly distributed in the range of 3–15 nm, with the secondary effect ascribed to the reduction of defects in the intercalated MT. However, the K for EMB@C_{16} is slightly reduced compared to that of MT@C_{16}. The subtle weakening effect could be due to the integration of the hydrocarbon/alkyl chain from the organic CTAB in MT, which causes an uneven distribution and an opaque nature in the EMB pore structure. In addition, the expanded pores in EMB presumably contribute to a high junction thermal resistance between hybrid components and an elevated interfacial thermal resistance within the composite skeleton. A similar phenomenon has been reported in nanoclay/graphene aerogel-supported lauric acid composite (Tang et al. 2024).

The shape stability of the phase change composites was investigated by subjecting the composite sample to repeated heating and cooling processes at 80 °C, and the dynamic change in the weight content of composite materials was calculated (Fig. 8d). The composite PCMs demonstrated high stability over 120 s heating cycles, with a leakage rate that was less than 3.1% of that of paraffin. SB@C_{16} exhibited a comparatively high leakage rate, whereas EMB@C_{16} exhibited a 2.2% lower leakage rate. The latter effectively inhibited the escape of liquefied paraffin while maintaining a nearly constant mass fraction after 100 s of heating, providing extra protection against seepage and alleviating large deformation through the 3D lattice backbones.

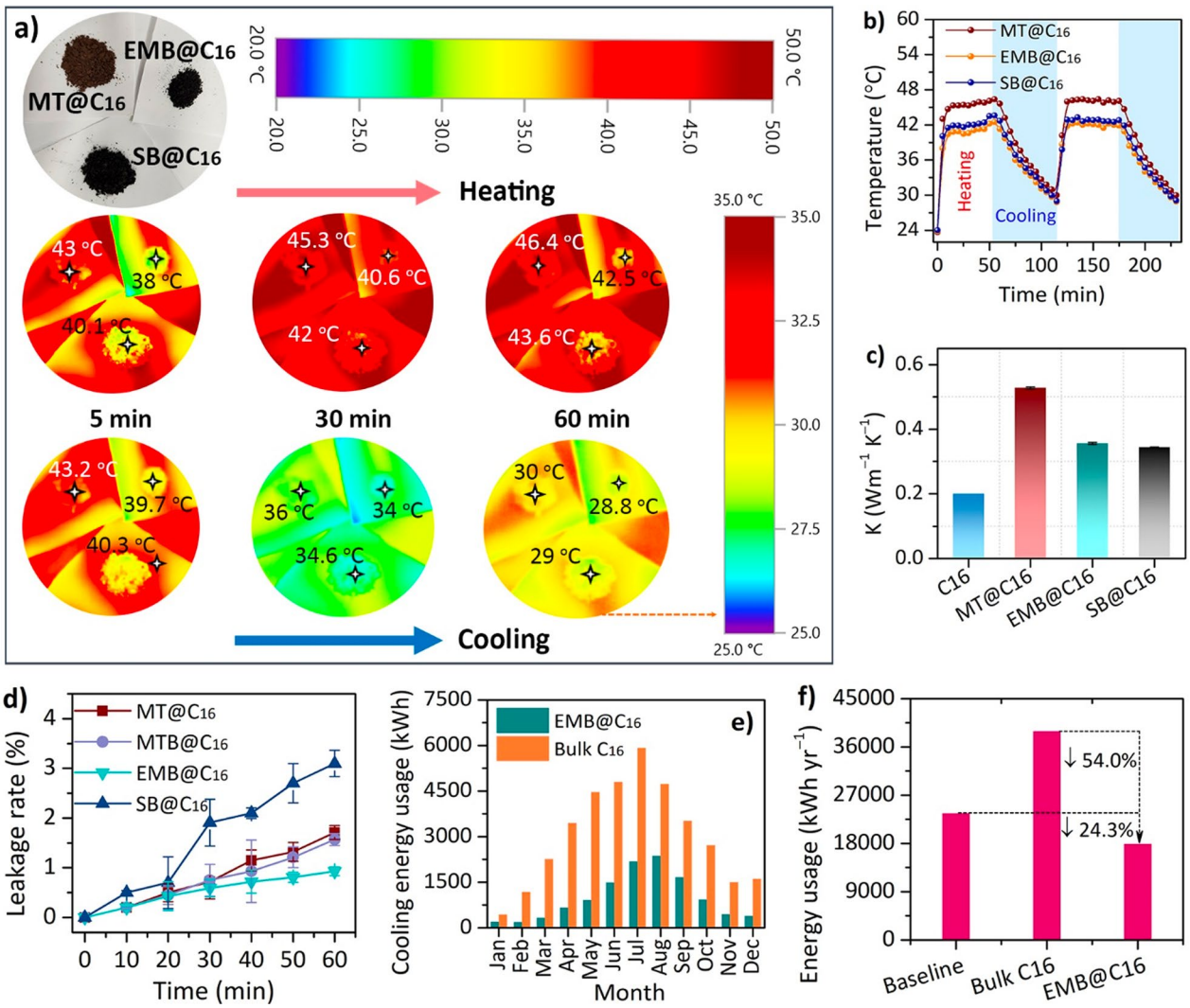

Fig. 8 Thermal management and thermophysical performance of fabricated composites. **a** IR thermal images of composite materials during heating–cooling, **b** Time–temperature curves of the heating–cooling cycles of SB@C_{16}, MT@C_{16}, and EMB@C_{16}. **c** Thermal conductivity performance, **d** Leakage rate properties of composite materials at 80 °C for 60 min heating, **e** Simulated cooling energy consumption (kWh), and **f** Annual energy consumption of bulk C_{16}, EMB@C_{16}, and baseline (without PCM)

The energy-saving performance of the as-prepared biobased phase change composite is essential from the standpoint of thermal buffering efficacy in building applications. To demonstrate its potential, DesignBuilder simulations were conducted using EMB@C_{16} and bulk C_{16} as building interior materials for a historic building in Seoul, South Korea (KOR-AF-HQ). As shown in Fig. 8e, the EMB@C_{16} composite exhibited superior cooling energy-saving performance compared to bulk C_{16}, which showed high energy consumption from April to Sep (summer season). It further achieved a total annual energy consumption reduction of 54.0% compared to bulk PCM (38,919.7 kWh) and 24.3% from the baseline (without PCM) (23,620.2 kWh) (Fig. 8f). This promising performance is ascribed to the engineered biomineral framework, which enhances the thermal charging and discharging process during phase transitions.

It is worth noting that, despite the substantial improvement in thermophysical properties, such as K and ΔH_m, the cost of the surfactant and the large volume of wastewater generated from washing and unreacted surfactants present major barriers for the scalable production of EMB. To overcome these limitations, a one-pot modification approach employing renewable, low-cost biobased surfactants (e.g., saponin glycosidic compounds) is proposed, which can be integrated with physical activation

techniques (e.g., milling) and supported by a closed-loop wastewater recycling system to enable sustainable and efficient process water reuse.

4 Conclusion

A novel biomineral-based phase-change thermal energy storage material was developed using liquid paraffin infusion in mineral and biochar through engineering with CTAB, ultrasonication, and vacuum-assisted encapsulation. The surface area and pore volume of the EMB enlarged abruptly, exhibiting an increase of approximately 516.4% compared with bulk MT, thereby providing a high PCM loading rate. Furthermore, the composites exhibited a melting enthalpy ranging between 15.7 and 121.3 J g^{-1}, with EMB@C_{16} demonstrating an enhancement of approximately 223.3% compared to MT@C_{16}, while also achieving high thermal stability between 120 and 160 °C without significant weight loss. The integration of engineered mineral-doped biochar composite PCMs as core energy storage circumvents the need to compromise on the complicated fabrication process, environmental concerns, and pore structure of PCM carriers. This approach also engineers the thermal transport pathways within the cavity wall, resulting in an enhanced thermal conductivity performance of EMB@C_{16} (thermal conductivity enhanced by 78% from the pristine PCM). In addition, the biomineral-based composite PCMs enhanced thermal insulation performance compared to the bulk MT@C_{16} composite, reducing thermal conductivity by more than 48.3%. Moreover, the latent heat of the phase change was retained after 1000 thermal cycles under both short and long heating–cooling times, with only a 4.1% reduction, demonstrating outstanding prolonged thermal management and energy storage capacity. The synergy of modified nanoclay and biochar created a 3D matrix-driven seepage resistance of pristine paraffinic PCM, with a less than 2.2% leakage rate of paraffin. Engineering and integration with biocarbons, which expand the pore adsorption capacity and shorten the hydrogen bonding interactions, were used for the synchronous enhancement of stability and crystallinity (0.98) in composite materials. Hence, the as-prepared phase-change hybrids, fabricated via an environmentally benign and facile process, offer considerable potential for diverse thermal regulation applications, such as building energy savings when used as an interior building materials supplement. Furthermore, the study supports promoting the circular economy through waste-to-resource utilization and advancing green energy storage development.

Supplementary Information

The online version contains supplementary material available at https://doi.org/10.1007/s42773-025-00517-4.

Supplementary Material 1.

Acknowledgements
Not applicable.

Author contributions
Writing–original draft, Conceptualization: Dimberu G. Atinafu. Resources, Visualization: Jihee Nam. Supervision, Funding acquisition: Sumin Kim. All authors read and approved the final manuscript.

Funding
This work was supported by the National Research Foundation of Korea (NRF) grant funded by the Korean Government (MSIT) (No. RS-2025-02263517).

Data availability
The datasets used or analyzed during the current study are available from the corresponding author upon reasonable request.

Declarations

Competing interests
The authors declare that they have no known competing financial interests or personal relationships that could have appeared to influence the work reported in this paper.

Author details
[1]Department of Architecture and Architectural Engineering, Yonsei University, Seoul 03722, Republic of Korea.

Received: 22 May 2025 Revised: 4 September 2025 Accepted: 8 September 2025
Published online: 09 January 2026

References

Aftab W, Shi J, Jin Y, Usman A, Qin M, Ashraf Z et al (2024) Phase engineered composite phase change materials for thermal energy manipulation. Small n/a(n/a):2312134. https://doi.org/10.1002/smll.202312134

Arif M, Liu G, ZiaurRehman M, Mian MM, Ashraf A, Yousaf B et al (2023) Impregnation of biochar with montmorillonite and its activation for the removal of azithromycin from aqueous media. Environ Sci Pollut Res 30(32):78279–78293. https://doi.org/10.1007/s11356-023-27908-z

Atinafu DG, Jin Chang S, Kim K-H, Kim S (2020) Tuning surface functionality of standard biochars and the resulting uplift capacity of loading/energy storage for organic phase change materials. Chem Eng J 394:125049. https://doi.org/10.1016/j.cej.2020.125049

Atinafu DG, Yun BY, Kim YU, Yang S, Wi S, Kim S (2021) Thermoconductive n-alkane enables ultra-high shape/thermal stability, durability, and ambient thermal energy harvesting. Chem Eng J 420:130374

Atinafu DG, Kim YU, Kim S, Kang Y, Kim S (2024a) Advances in biocarbon and soft material assembly for enthalpy storage: fundamentals, mechanisms, and multimodal applications. Small 20(13):2305418

Atinafu DG, Choi JY, Yun BY, Nam J, Kim HB, Kim S (2024b) Energy storage and key derives of octadecane thermal stability during phase change assembly with animal manure-derived biochar. Environ Res 240:117405

Batra R, Purwar R, Kulanthaivel S, Mishra P (2021) Cetyl trimethyl ammonium bromide modified Montmorillonite-doped Tasar silk fibroin/Polyvinyl alcohol blend 3D nanowebs for tissue engineering applications. Macromol Mater Eng 306(11):2100450

Chen R, Li D, Sheng N, Zhu C (2024) Direct synthesis of porous aluminum nitride foams for enhancing heat transfer and anti-leakage performance of phase change materials. Thermochim Acta 734:179706. https://doi.org/10.1016/j.tca.2024.179706

Dixit P, Vennapusa JR, Parvate S, Singh J, Dasari A, Chattopadhyay S (2021) Thermal buffering performance of a propyl palmitate/expanded perlite-based form-stable composite: experiment and numerical modeling in a building model. Energy Fuels 35(3):2704–2716. https://doi.org/10.1021/acs.energyfuels.0c03553

Gao H, Wang J, Chen X, Wang G, Huang X, Li A, Dong W (2018) Nanoconfinement effects on thermal properties of nanoporous shape-stabilized composite PCMs: a review. Nano Energy 53:769–797

Geng X, Qin M, Shen Z, Xiong F, Di J, Yang C et al (2024) Muscle-inspired super-flexible phase change materials with programmable deformation for photothermal actuation. Adv Funct Mater. https://doi.org/10.1002/adfm.202418848

Guo W, Chen H, Li G, Zheng Y, Qi L (2025) Eco-friendly biochar/CNTs-enhanced myristic acid composite phase change materials for efficient solar-thermal energy conversion. Sol Energy 294:113483

Ishak S, Yio M, Moon J, Mandal S, Sasui S, Abdul Shukor Lim NH et al (2025) Hydration and microstructural development of cement pastes incorporating diatomaceous earth, expanded perlite, and shape-stabilized phase change materials (SSPCMs). Constr Build Mater 468:140483

Jeong S-G, Jin Chang S, We S, Kim S (2015) Energy efficient thermal storage montmorillonite with phase change material containing exfoliated graphite nanoplatelets. Solar Energy Mater Solar Cells 139:65–70. https://doi.org/10.1016/j.solmat.2015.03.010

Kang X, You Z, Huang Y, Peng J, He T, Su T et al (2025) New insights in the formation mechanism of cellulose-based biochar. Small. https://doi.org/10.1002/smll.202410597

Karaipekli A, Sarı A (2009) Capric–myristic acid/vermiculite composite as form-stable phase change material for thermal energy storage. Sol Energy 83(3):323–332

Kassem I, Ablouh E-H, El Bouchtaoui F-Z, Hannache H, Ghalfi H, Sehaqui H, El Achaby M (2022) Cellulose nanofibers/engineered biochar hybrid materials as biodegradable coating for slow-release phosphate fertilizers. ACS Sustain Chem Eng 10(46):15250–15262. https://doi.org/10.1021/acssuschemeng.2c04953

Lee J, Han H, Noh D, Lee J, Lim DD, Park J et al (2024) Multiscale porous architecture consisting of graphene aerogels and metastructures enabling robust thermal and mechanical functionalities of phase change materials. Adv Funct Mater 34(42):2405625

Lehmann J, Cowie A, Masiello CA, Kammann C, Woolf D, Amonette JE et al (2021) Biochar in climate change mitigation. Nat Geosci 14(12):883–892. https://doi.org/10.1038/s41561-021-00852-8

Li C, Fu L, Ouyang J, Yang H (2013) Enhanced performance and interfacial investigation of mineral-based composite phase change materials for thermal energy storage. Sci Rep 3:1908

Li M, Guo Q, Nutt S (2017) Carbon nanotube/paraffin/montmorillonite composite phase change material for thermal energy storage. Sol Energy 146:1–7. https://doi.org/10.1016/j.solener.2017.02.003

Li B-X, Luo Z, Yang W-G, Sun H, Ding Y, Yu Z-Z, Yang D (2023a) Adaptive and adjustable MXene/reduced graphene oxide hybrid aerogel composites integrated with phase-change material and thermochromic coating for synchronous visible/infrared camouflages. ACS Nano 17(7):6875–6885. https://doi.org/10.1021/acsnano.3c00573

Li Z-R, Hu N, Fan L-W (2023b) Nanocomposite phase change materials for high-performance thermal energy storage: a critical review. Energy Storage Mater 55:727–753

Li Y, Zhao X, Tang Y, Zuo X, Yang H (2024) Mineral-based composite phase change materials assembled into 3D ordered aerogels for efficient wearable filtration and thermal management. Adv Funct Mater 34(39):2403059

Li Y, Feng Y, Qin M, Chen K, An Y, Liu P et al (2025) Co-anchored hollow carbonized kapok fiber encapsulated phase change materials for upgrading photothermal utilization. Small. https://doi.org/10.1002/smll.202500479

Liao C-Y, Chiou J-Y, Lin J-J (2017) Phase change materials of fatty amine-modified silicate clays of nano layered structures. RSC Adv 7(38):23530–23534. https://doi.org/10.1039/C7RA02876H

Liu Z, Lyu J, Fang D, Zhang X (2019) Nanofibrous Kevlar aerogel threads for thermal insulation in harsh environments. ACS Nano 13(5):5703–5711. https://doi.org/10.1021/acsnano.9b01094

Liu H, Guo C, Cui Y, Yin J, Li S (2022) Experimental and modeling investigation of organic modified montmorillonite with octyl quaternary ammonium salt. Sci Rep 12(1):14305. https://doi.org/10.1038/s41598-022-18253-1

Liu L, Zhang Y, Zhang S, Tang B (2023) Advanced phase change materials from natural perspectives: structural design and functional applications. Adv Sci 10(22):2207652

Liu X, Zhao X, Tang Y, Yang H (2024) Hierarchical porous silicon-carbon encapsulated phase change materials for efficient photothermoelectric conversion. ACS Appl Mater Interfaces 16(51):70498–70507. https://doi.org/10.1021/acsami.4c14073

Liu X, Lin F, Guo Z, Liu M, Jiang Y, Qiao J et al (2025a) Diatomite porous ceramic-based phase change materials with Ti3C2Tx coating for efficient solar-thermal energy conversion. J Energy Storage 107:114967

Liu X, Hou X, Yan L, Zhang Y, Wang J-J (2025b) ZnO functionalized paraffin/diatomite phase change material and its thermal management mechanism in PDMS coatings. RSC Adv 15(8):6032–6042. https://doi.org/10.1039/D4RA08017C

Lv L, Huang S, Zhou H (2024) Performance investigation of biochar/paraffin composite phase change materials in latent heat storage systems: feasibility of biochar as a thermal conductivity enhancer. J Energy Storage 91:112106

Qian T, Li J, Min X, Guan W, Deng Y, Ning L (2015) Enhanced thermal conductivity of PEG/diatomite shape-stabilized phase change materials with Ag nanoparticles for thermal energy storage. J Mater Chem A 3(16):8526–8536. https://doi.org/10.1039/C5TA00309A

Qiu L, Wang Z, Liu Z, Li H, Feng Y (2025) Nanopore confinement-driven synchronous enhancement of thermal and mechanical properties of phase change materials. Angewandte Chemie Int Edition. https://doi.org/10.1002/anie.202500957

Shen Y, Gu J, Zhu Z, Zhang L, Lv X-J, Li Y (2025) Fast Li+ de-solvation kinetics with PDDA intercalated-montmorillonite hybrid artificial interface layer on Cu substrate for lithium metal batteries in a wide climate temperature. Adv Funct Mater 35(6):2414835. https://doi.org/10.1002/adfm.202414835

Shi Z, Li P, Liu L (2023) Interactions between CTAB and montmorillonite by atomic force microscopy and molecular dynamics simulation. Colloids Surf A Physicochem Eng Asp 657:130656

Tang Y, Zhao X, Li Y, Yang Z, Zuo X, Tang A, Yang H (2024) Nanoclay hybridized graphene aerogels encapsulating phase change material for efficient solar-driven desalination and electricity generation. Adv Funct Mater 34(48):2408693

Wang J, Yang M, Lu Y, Jin Z, Tan L, Gao H et al (2016) Surface functionalization engineering driven crystallization behavior of polyethylene glycol confined in mesoporous silica for shape-stabilized phase change materials. Nano Energy 19:78–87

Wang G, Liu L, Hu X, Hu P, Li M, Zhang X, Wang J (2025) Aerogel-functionalized phase change materials toward lightweight and robust thermal management. Small Methods. https://doi.org/10.1002/smtd.202500127

Wu H, Hu X, Li X, Sheng M, Sheng X, Lu X, Qu J (2022) Large-scale fabrication of flexible EPDM/MXene/PW phase change composites with excellent light-to-thermal conversion efficiency via water-assisted melt blending. Compos Part A Appl Sci Manuf 152:106713

Xi S, Wang M, Wang L, Xie H, Yu W (2021) 3D reduced graphene oxide aerogel supported TiO2-x for shape-stable phase change composites with high photothermal efficiency and thermal conductivity. Solar Energy Mater Solar Cells 226:111068. https://doi.org/10.1016/j.solmat.2021.111068

Xiong X, Yu IKM, Chen SS, Tsang DCW, Cao L, Song H et al (2018) Sulfonated biochar as acid catalyst for sugar hydrolysis and dehydration. Catal Today 314:52–61

Xue T, Peng L, Liu C, Li R, Qiu R, Qian Y et al (2025) Synthesis of high quality two dimensional covalent organic frameworks through a self-sacrificing guest strategy. Nat Commun 16(1):2023. https://doi.org/10.1038/s41467-025-57311-w

Yang Z, Jia S, Niu Y, Lv X, Fu H, Zhang Y et al (2021) Bean-pod-inspired 3D-printed phase change microlattices for solar-thermal energy harvesting and storage. Small 17(30):2101093

Yang W, Xia X, Liu X, Zhang S (2023) Interlayer structure and dynamic properties of CTMAB–montmorillonite: experiment and molecular dynamics. RSC Adv 13(19):13324–13336. https://doi.org/10.1039/D3RA01834B

Yang X, Hou Z, Yang X, Li M, Guo Y, Wang K et al (2025) Efficient removal of cationic malachite green using co-pyrolyzed corn straw biochar-montmorillonite composites. J Environ Manage 375:124224

Yin Q, Zhu G, Wang R, Zhao Z (2024) Enhancement of the thermal properties of the phase change composite of acid-base modified biochar/paraffin wax. Solar Energy Mater Solar Cells 269:112802

Yu Y, Wei L, Pang Z, Wu J, Dong Y, Pan X et al (2024) Multifunctional wood composite aerogel with integrated radiant cooling and fog-water harvesting for all-day building energy conservation. Adv Funct Mater. https://doi.org/10.1002/adfm.202414590

Yuan K, Gao C, Zhao G, Yang H (2024) Electronic interaction between biochar and montmorillonite toward enhanced peroxymonosulfate activation. Appl Clay Sci 249:107260

Zhang X, Li X, Zhou Y, Hai C, Shen Y, Ren X, Zeng J (2018) Calcium chloride hexahydrate/diatomite/paraffin as composite shape-stabilized phase-change material for thermal energy storage. Energy Fuels 32(1):916–921. https://doi.org/10.1021/acs.energyfuels.7b02866

Zhu Z, Bashir A, Wu X, Liu C, Zhang Y, Chen N et al (2025) Highly integrated phase change and radiative cooling fiber membrane for adaptive personal thermal regulation. Adv Funct Mater 35(9):2416111